Differentiating the Degradation Phenomena in Silicon-Graphite Electrodes for Lithium-Ion Batteries

Morten Wetjen,[a,*,z] Daniel Pritzl,[a,*] Roland Jung,[a,*] Sophie Solchenbach,[a,*] Reza Ghadimi,[b] and Hubert A. Gasteiger[a,]**

[a] *Chair of Technical Electrochemistry, Department of Chemistry and Catalysis Research Center, Technical University of Munich, D-85748 Garching, Germany*
[b] *JEOL (Germany) GmbH, D-85356 Freising, Germany*

Silicon-graphite electrodes usually experience an increase in cycling performance by the addition of graphite, however, the relation of the silicon/graphite ratio and the aging mechanisms of the individual electrode and electrolyte compounds still requires a more fundamental understanding. In this study, we present a comprehensive approach to understand and quantify the degradation phenomena in silicon-graphite electrodes with silicon contents between 20-60 wt%. By evaluating the cycling performance and total irreversible capacity of silicon-graphite electrodes vs. capacitively oversized $LiFePO_4$ electrodes in presence of a fluoroethylene carbonate (FEC)-containing electrolyte, we demonstrate that the aging of silicon-based electrodes can be distinguished into two distinct phenomena, which we describe as silicon particle degradation and electrode degradation. Cross-sectional scanning electron microscopy (SEM) images and a detailed analysis of the electrode polarization upon cycling complement our discussion. Further, we deploy post-mortem ^{19}F-NMR spectroscopy to (i) quantify to loss of moles of FEC in the electrolyte and correlate this with the amount of charge that was exchanged by the silicon-graphite electrodes, (ii) estimate the pore volume of the silicon-graphite electrodes that is occupied by FEC decomposition products, and (iii) derive implications for the relation of the electrolyte volume and cycle life of commercial silicon-based Li-ion batteries.

Manuscript submitted June 26, 2017; revised manuscript received September 5, 2017. Published September 19, 2017. This was Paper 280 presented at the Honolulu, Hawaii, Meeting of the Society, October 2–7, 2016.

Silicon-based electrodes are very promising candidates to enable the next generation of Li-ion batteries with energy densities on the cell level beyond 350 Wh kg^{-1}.[1,2] In contrast to conventional intercalation anode materials, such as graphite (LiC_6, 372 mAh g^{-1}, 890 Ah L^{-1}), the specific capacity of silicon alloy electrodes is significantly higher ($Li_{15}Si_4$, 3579 mAh g^{-1}, 2194 Ah L^{-1}).[3] Nonetheless, commercialization of silicon-based electrodes is still hampered because of two major challenges:[4]

(i) Large volume expansions up to 280% upon repeated (de-)lithiation of silicon particles deteriorate the electrode integrity, thus causing isolation of active material.[5–7] The formerly reported pulverization of micron-sized silicon particles due to mechanical stress upon repeated volume expansion has been partially solved by using nanometer-sized particles. However, reduction of the silicon particle size also leads to inferior electronic conduction due to more numerous interparticle contacts, and higher solid-electrolyte-interphase (SEI) losses due to the larger relative surface area.[8–10]

(ii) Continuous side reactions at the silicon/electrolyte interface caused by repeated volume expansion and contraction result in ongoing electrolyte decomposition and in a gradual loss of active lithium.[8] In the course of this, SEI-forming additives in the electrolyte, e.g., FEC, are depleted, which was shown to result in a significant increase in cell polarization and a concomitant rapid capacity drop.[8,11]

Various strategies have been proposed to overcome the detrimental effects associated with the volume expansion during (de-)lithiation of silicon and to reduce concomitant irreversible capacity losses, including preparation of silicon thin-films with a significantly reduced silicon/electrolyte interface,[6,12–14] Si-Al-Fe active/inactive alloy electrodes that reduce the volume expansion of the active phase,[5,15,16] and design of nanostructured silicon materials with carbonaceous compounds, such as graphite, to improve the electrical conductivity within the electrode and to better accommodate the volume expansion of silicon.[17–20] Although the surface area per capacity usually increases for nanostructured silicon materials with decreasing diameter,[21] which leads to a higher first cycle irreversible capacity loss, silicon nanowires offer the advantage of a smaller relative surface area change upon (de-)lithiation and in addition usually reveal less morphological changes, due to a reduced mechanical stress within the materials.[22] Therefore, irreversible capacity losses upon cycling are expected to be lower compared to conventional nanoparticles.

Further studies on the degradation mechanisms of silicon-based electrodes were performed with respect to the actual conditions in commercial Li-ion batteries. While some research groups, including those from Obrovac,[15] Guyomard,[23,24] and Abraham,[25–27] already reported studies on full-cell configurations, the majority of the academic literature still refers to half-cell measurements, using lithium metal counter electrodes and an excess of electrolyte. However, side reactions at the lithium metal/electrolyte interface and the usually 10 times larger amount of electrolyte (i.e. >50 µL cm^{-2} instead of 5 µL cm^{-2} in commercial cells)[11] make it difficult to evaluate the degradation phenomena occurring at the silicon-based electrode, including the loss of active lithium and depletion of the electrolyte.[28–30]

In this study, we present a comprehensive approach to understand the degradation mechanisms in silicon-graphite electrodes. Hence, we prepare silicon-graphite electrodes with practical areal capacities between 1.8 and 2.3 mAh cm^{-2}, composed of physical mixtures of different silicon/graphite active material ratios, with silicon contents between 20–60 wt%.[31] By use of cyclic voltammetry, we investigate the electrochemical (de-)lithiation of silicon and graphite as a function of the active material ratio. To evaluate the electrode degradation upon cycling, we introduce pseudo-full cells, comprising silicon-graphite negative electrodes and capacitively oversized $LiFePO_4$ positive electrodes. This cell configuration offers several advantages over practical full-cells, namely: (i) a stable reference potential of 3.45 V vs. Li/Li$^+$ to monitor the silicon-graphite potential in a two-electrode coin-cell configuration, and (ii) to provide a defined lithium reservoir, which allows to investigate exclusively the degradation of the silicon-graphite electrode without an additional capacity loss due to the depletion of cyclable lithium. While these conditions would also be satisfied by a lithium metal electrode, the third reason is (iii) to minimize side reactions of the electrolyte at the positive electrode (here: $LiFePO_4$), which would alter the electrolyte (and FEC) decomposition and thus influence its quantification. As electrolyte we use 1 M $LiPF_6$ in EC:EMC (LP57) with 5 wt% of the widely used fluoroethylene carbonate (FEC) as additive, which is known to significantly improve the cycling stability of the silicon-graphite

*Electrochemical Society Student Member.
**Electrochemical Society Fellow.
[z]E-mail: morten.wetjen@tum.de

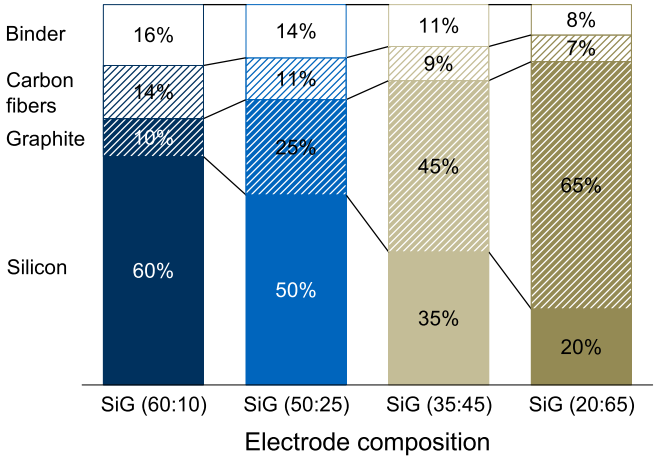

Scheme 1. Silicon-graphite electrode compositions (in wt%) that were investigated in this study.

electrode.[32] We also added a comparably large amount of electrolyte to the coin cells (130 µL or 84 µL cm^{-2}; ~15 times larger compared to large-scale cells), because it allows for a more precise quantification of the FEC consumption via ^{19}F-NMR.[11] From the analysis of the differential capacity curves and the electrode polarization upon cycling, we deconvolute the different degradation mechanisms arising from silicon-graphite electrodes. In addition, we evaluate the consumption of FEC as primary source for electrolyte decomposition through ^{19}F-NMR analysis of the electrolyte harvested from coin-cells after 120 cycles. Finally, we discuss the implications of these results on commercial Li-ion batteries with silicon-based electrodes by estimating the volume of the electrolyte decomposition products and forecasting cycle lifetimes, taking into account practical electrolyte amounts.

Experimental

Electrode preparation.—Silicon-graphite (SiG) electrodes, consisting of silicon nanoparticles (~200 nm, silicon, Wacker Chemie AG, Germany) and graphite (~20 µm, T311, SGL Carbon GmbH, Germany), were prepared through an aqueous ink procedure. Hence, silicon and graphite were thoroughly mixed with vapor grown carbon fibers (VCGF-H, Showa Denko, Japan) and lithium poly(acrylate) (LiPAA, MW = 250,000 g mol^{-1}, Sigma-Aldrich, Germany) in a planetary ball mill (Pulverisette 7, Fritsch, Germany) with ZrO_2 balls (10 mm diameter) under stepwise addition of 18 MΩ cm Milli-Pore water (final solid content ~30 wt%). The resulting ink was cast onto Cu-foil (thickness 25 µm, Goodfellow, USA), using a gap bar coater (RK PrintCoat Instruments, UK). Electrode discs of 14 mm in diameter were punched out and were subsequently dried in a Büchi oven for at least 12 h at 100°C, before being transferred into an Ar atmosphere MBraun glove box (H_2O and O_2 concentration <0.1 ppm) without exposure to air. The areal capacity of the resulting SiG electrodes ranged from 1.8 to 2.3 mAh cm^{-2}, which corresponds to a silicon-graphite active material loading of 0.71–1.84 mg_{SiG} cm^{-2}, depending on the active material ratio.

Scheme 1 summarizes the electrode compositions that were investigated in this study. As one can see, the weight contribution of the active materials (silicon and graphite) accounted for 70–85 wt% of the total electrode mass. Herein, the fraction of silicon was stepwise decreased from 60 to 20 wt%, while the fraction of graphite was simultaneously increased from 10 to 65 wt%. To accomplish adequate electrode integrity and to maintain sufficient electrical conductivity upon cycling, the amount of conductive additive and binder were adjusted to the amount of silicon in the electrode. In accordance with Marks et al.,[33] we adjusted the binder coverage to ~6.3 mg m_{BET}^{-2} in all compositions, considering a BET surface area of ~40 m^2 g^{-1} for silicon in the delithiated state, ~5 m^2 g^{-1} for graphite, and ~13 m^2 g^{-1} for the carbon fibers. During the optimization of the electrode compositions, we explored different binder and conductive carbon contents that affected the integrity and cycling stability of the electrodes to a certain extent; yet they did not impact the relation of the FEC consumption and the exchanged capacity, as will be explained in detail in the Discussion section. As the theoretical electrode capacities ranged from 960 to 2,200 mAh g^{-1}_{el} (taking theoretical active material capacities of 372 mAh g^{-1}_{C} and 3579 mAh g^{-1}_{Si}),[21] the electrode coating thicknesses were adjusted to 15-31 µm (measured by Mitutoyo *Litematic VL-50*, Japan), thus providing a consistent areal capacity of 1.8–2.3 mAh cm^{-2}.

Electrolyte and test cell assembly.—Electrochemical characterization was performed in coin-cells (CR2032, Hohsen, Japan) that were assembled in an Ar-filled glove box (MBraun, Germany) by sandwiching two porous glass fiber separators (Ø 16 mm, thickness 250 µm, VWR, USA) soaked with 130 µL electrolyte solution (i.e., 84 µL cm^{-2}) between a silicon-graphite electrode (Ø 14 mm, 1.8–2.3 mAh cm^{-2}) and either a lithium metal electrode (Ø 15 mm, 450 µm thickness, Rockwood Lithium, USA) for cyclic voltammetry or a capacitively oversized $LiFePO_4$ (LFP) electrode (Ø 15 mm, 3.5 mAh cm^{-2}, Custom cells, Germany) for cell cycling. As electrolyte solution, 1 M $LiPF_6$ dissolved in a mixture of ethylene carbonate (EC) and ethyl methyl carbonate (EMC) (3:7 w:w; LP57, BASF, Germany) and 5 wt% of fluoroethylene carbonate (FEC, BASF, Germany) was used.

Electrode morphology.—The morphology of the pristine silicon-graphite electrodes was investigated by scanning electron microscopy (SEM). First, electrode cross-sections were prepared by Argon ion beam polishing, using a JEOL Cross Section Polisher IB-09010CP (JEOL, Japan). Afterwards, SEM images were measured by use of a JEOL JSM-7800F PRIME (JEOL, Japan) with a field-emission electron source and a secondary electron detector.

Cyclic voltammetry.—The electrochemical (de-)lithiation of the SiG electrodes was characterized by cyclic voltammetry in a Li//SiG coin-cell setup. Alternating linear potentiodynamic sweeps with a scan rate of 25 µV s^{-1} were applied, forcing the cell potential from open circuit potential (typically ~2.6 V vs. Li/Li^+) to 0.01 V vs. Li/Li^+ (lower vertex potential) and then back to 1.5 V vs. Li/Li^+ (upper vertex potential). All measurements were performed in a climate chamber (Binder, Germany) at 25°C (±0.5°C), using a multi-channel potentiostat VMP3 (BioLogic, France).

Cell cycling.—Electrode polarization and cycling performance of SiG electrodes were investigated through galvanostatic cycling of SiG//$LiFePO_4$ coin-cells. Initially, a formation cycle between 0.01 and 1.25 V vs. Li/Li^+ (corresponding to 3.44 and 2.2 V cell voltage) was applied to all cells using a C-rate of 0.05 h^{-1} (~0.1 mA cm^{-2}). Two constant voltage (CV) steps were performed at the end of SiG lithiation/delithation (i.e., at 0.01/1.25 V vs. Li/Li^+) with a current limit of 0.02 h^{-1}. For the subsequent cycles, the C-rate was increased to 0.5 h^{-1} (~1.0 mA cm^{-2}). All measurements were performed in a climate chamber (Binder, Germany) at 25°C (±0.5°C), using a battery cycler (Series 4000, Maccor, USA).

Electrolyte consumption.—Consumption of fluoroethylene carbonate (FEC) during galvanostatic cycling was investigated by ^{19}F-NMR spectra which were obtained post-mortem from the electrolyte solutions. For this, SiG//$LiFePO_4$ coin-cells were disassembled after 120 cycles and the glass fiber separators were subsequently dipped into deuterated dimethyl sulfoxide (DMSO-d6, anhydrous, Sigma-Aldrich, USA). The resulting solutions were then filled into air-tight NMR tubes and ^{19}F-NMR spectra were measured using a Bruker Ascend 400 (400 MHz). As described by Jung et al., the resulting ^{19}F-NMR spectra show only peaks that can either be ascribed to PF_6^- or FEC, i.e., no additional peaks from $PO_2F_2^-$ or PO_3F^{2-} can be observed that originate from salt decomposition or separator

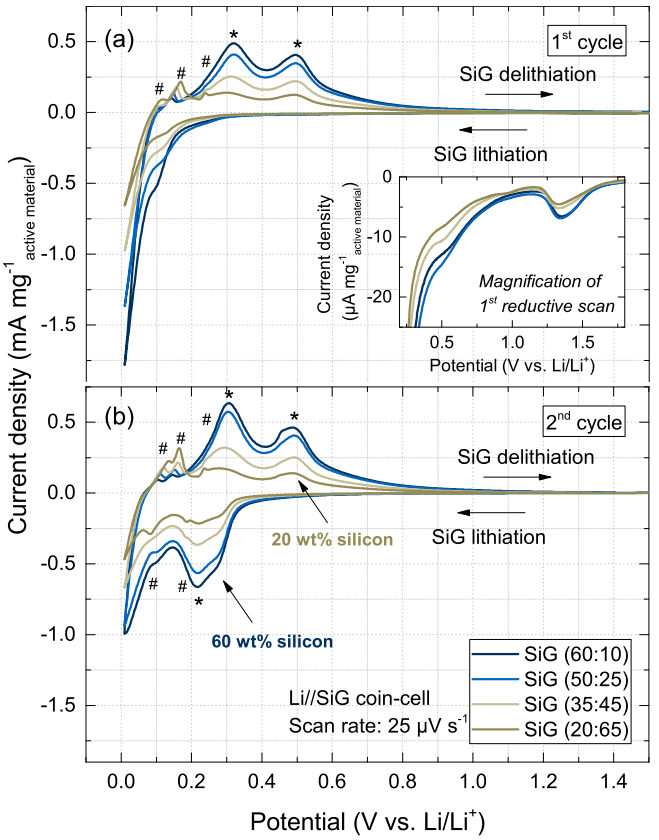

Figure 1. Cyclic voltammetry responses of the first (panel a) and the second cycle (panel b) of Li//SiG coin-cells, incorporating silicon-graphite electrodes with different active material ratios. Characteristic features are labelled either by star (silicon) or hash (graphite). Electrolyte: 130 μL LP57 with 5 wt% FEC, scan rate: 25 μV s^{-1}, vertex potentials: 0.01 and 1.5 V, electrode area: 1.54 cm^2, areal capacities ranged from 1.8 to 2.3 mAh cm^{-2}, temperature: 25°C.

decomposition by HF.[11,34] As a result, the concentration of PF_6^- in the electrolyte solution shows no quantitative changes upon cycling and can thus be defined as an internal standard. For that reason, changes in the ratio of PF_6^- peak integrals to FEC peak integrals allow to monitor the consumption of FEC after a selected number of cycles. A previous work from our group,[11] which deployed this method provided the same four-electron mechanism for the reduction of FEC as an independently conducted analysis via gas chromatography coupled with mass spectrometry (GC-MS) by Petibon et al.[35]

Results

Electrode characterization.—Table I summarizes the properties of the silicon-graphite electrodes that were investigated in this study. Based on measured areal loadings of the electrode coatings, the known electrode composition, and the measured electrode thicknesses, the calculated electrode densities of all electrodes range between ~0.6–0.7 g cm^{-3}_{el}, corresponding to electrode porosities ranging in between ~67–73%, were obtained for all compositions. We ascribe this characteristic to a combination of the similar bulk densities of silicon (~2.3 g cm^{-3}) and graphite (~2.2 g cm^{-3}) and of the large and well dispersed carbon fibers (diameter: 150 nm, length: 10–20 μm) that create a substantial amount of void spaces.

The electrochemical (de-)lithiation of the silicon-graphite electrodes was investigated by cyclic voltammetry. Figure 1 shows the current responses of (a) the first and (b) the second cycle obtained from the different SiG electrode compositions. While the lithiation features of silicon and graphite are largely superimposed during the first reductive scan at potentials below 0.18 V vs. Li/Li^+, the oxidative scan clearly reveals two characteristic delithiation peaks of silicon at 0.31 and 0.50 V vs. Li/Li^+,[36] as well as three delithiation peaks of graphite at 0.11, 0.16, and 0.24 V vs. Li/Li^+, which correspond to the voltage plateaus of lithium-graphite intercalation compounds LiC_x.[37] The silicon features appear more pronounced in the 60 wt% and 50 wt% silicon electrodes (blue curves), whereas the graphite peak currents decrease, according to the lower graphite content in these electrodes. As expected, the lithiation behavior of silicon changes between the first and second cycle (see Figure 1b). Once the silicon has become amorphous after the first reductive scan, lithiation in subsequent scans starts at more positive potentials of about 0.21 V and continues below 0.11 V vs. Li/Li^+. In agreement with Fuchsbichler et al.,[17] graphite is lithiated (<0.19 V vs. Li/Li^+) and delithiated (<0.24 V vs. Li/Li^+) step-wise at slightly more negative potentials compared to silicon.

The inset in Figure 1a shows a magnification of the first reductive scan. The feature at about 1.3 V vs. Li/Li^+ can be assigned to the reductive decomposition of FEC.[38] As it was reported earlier in the literature, FEC is reduced at more positive potentials than EC and EMC, thereby forming an SEI layer on the active material particles, which significantly reduces further electrolyte decomposition.[39–41]

Cycling performance in SiG//LFP cells.—The cycling performance of the silicon-graphite electrodes (1.8–2.3 mAh cm^{-2}) was investigated vs. capacitively oversized $LiFePO_4$ electrodes (~3.5 mAh cm^{-2}). To fully utilize the theoretical specific capacity of the different silicon-graphite electrodes, the cutoff potentials were set to 0.01 V vs. Li/Li^+ during lithiation (3.44 V cell voltage) and 1.25 V vs. Li/Li^+ during delithiation (2.2 V cell voltage). In addition, constant voltage steps were applied at the end of lithiation and delithiation. Figure 2 shows (a) the coulombic efficiency (in %) and (b) the gravimetric delithiation capacities normalized to the entire electrode mass (in mAh g^{-1}_{el}) as a function of the cycle number. Table I summarizes relevant data of the first cycle and the capacity retention upon

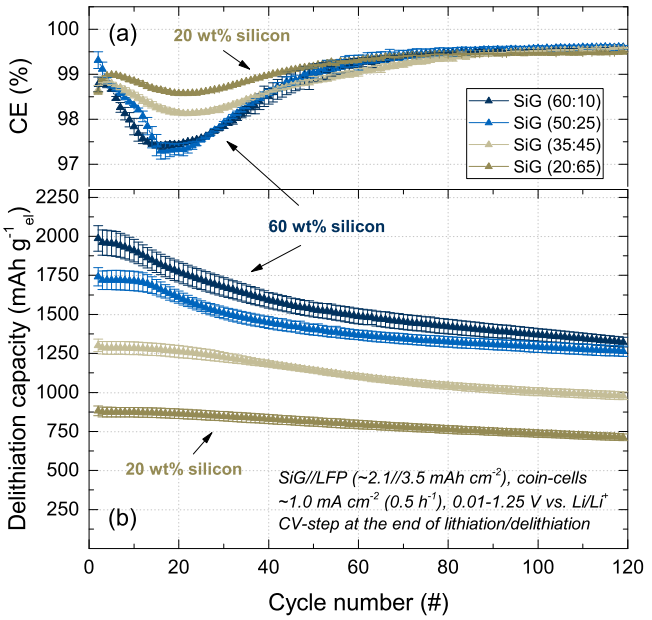

Figure 2. Galvanostatic cycling of SiG//LFP coin-cells, with different silicon-graphite electrode compositions. Areal capacities: SiG (1.8-2.3 mAh cm^{-2}), LFP (~3.5 mAh cm^{-2}), electrolyte: 130 μL LP57 with 5 wt% FEC, applied currents: ~0.1 mA cm^{-2} (0.05 h^{-1}) during formation cycle and ~1.0 mA cm^{-2} (0.5 h^{-1}) during consecutive cycles, SiG electrode cutoff potentials of 0.01 and 1.25 V vs. Li/Li^+, constant voltage steps at 0.01/1.25 V vs. Li/Li^+ at the end of (de-)lithiation with a current limit of 0.02 h^{-1}. Panel (a): Coulombic efficiency obtained from the ratio of delithiation/ lithiation capacity, and panel (b): Delithiation capacity in mAh g^{-1}_{el} per silicon-graphite electrode. The error bars represent the standard deviation of at least two independent repeat measurements.

Table I. Properties of the silicon-graphite electrodes that were investigated in this study. Selected data from the first galvanostatic cycle at 0.05 h^{-1} between 0.01 and 1.25 V vs. Li/Li^+ and from ^{19}F-NMR FEC consumption measurements after 120 cycles. The ± values represent the standard deviation of at least two independent repeat measurements.

		Electrode composition			
Electrode properties	Units	SiG (60:10)	SiG (50:25)	SiG (35:45)	SiG (20:65)
Theoretical electrode capacity	mAh g^{-1}_{el}	2,185	1,883	1,420	958
Capacity contribution from silicon	%	98.3	95.1	88.2	74.7
Areal capacity	mAh cm^{-2}	2.3 ± 0.2	1.8 ± 0.2	1.8 ± 0.2	2.1 ± 0.2
Electrode mass loading	mg cm^{-2}	1.06	0.94	1.30	2.17
Active material loading	mg_{SiG} cm^{-2}	0.74	0.71	1.04	1.84
Electrode thickness	µm	15 ± 2	16 ± 2	21 ± 2	31 ± 2
Electrode density	g cm^{-3}_{el}	0.71	0.59	0.62	0.70
Electrode porosity	%	67	73	72	68
Electrode BET area (delithiated)	m^2_{BET} g^{-1}	26	23	17	12
Binder coverage	mg m^{-2}_{BET}	6.1	6.2	6.3	6.6
1st cycle coulombic efficiency	%	87.6 ± 0.8	86.1 ± 0.7	86.3 ± 0.5	87.1 ± 0.5
1st cycle irreversible capacity	mAh_{irr} g^{-1}_{el}	272	272	201	128
1st cycle delithiation capacity	mAh g^{-1}_{el}	1,933	1,685	1,265	860
Capacity retention in cycle 120	mAh g^{-1}_{el}	1,323	1,264	979	713
Capacity retention cycle 3–120	%	67	74	76	82
cycle # at 80% capacity retention	#	44	58	87	>120
Total irreversible capacity after 120 cycles	Ah_{irr} g^{-1}_{el}	2.47	2.17	1.62	0.93
	mAh_{irr} cm^{-2}	2.62	2.04	2.11	2.02
Capacity per FEC after 120 cycles	mAh_{tot} µmol^{-1}	11.5	12.9	14.5	15.7
	$mAh_{tot, Si}$ µmol^{-1}	11.3	12.2	12.8	11.7
FEC per irreversible capacity after 120 cycles	µmol mAh^{-1}_{irr}	13.0	12.3	11.5	13.1

cycling. As can be seen from Figure 2b, the different electrode compositions demonstrate delithiation capacities between 860 mAh g^{-1}_{el} (20 wt% silicon, dark brown curve) and 1,930 mAh g^{-1}_{el} (60 wt% silicon, dark blue curve) during the first cycle (see also Table I). Interestingly, all electrodes indicate a very similar first cycle capacity utilization and coulombic efficiency, both in the range of ∼85–88%, independent of the electrode composition (i.e., all electrodes reveal a similar areal irreversible capacity loss of 0.28 ± 0.02 mAh cm^{-2} in the first cycle). These first cycle coulombic efficiencies of the SiG electrodes are very similar as for the silicon electrodes without graphite but using the same silicon particles (40 wt% silicon, 20 wt% VGCF, 20 wt% LiPAA) with 85–86% (data not shown), and are only slightly lower compared to the ∼92% for pure graphite electrodes (95 wt% graphite, 5 wt% PVdF). We explain this behavior by the similar BET surface area per capacity of both active materials (11–13 m^2_{BET} Ah^{-1}) in the delithiated state, suggesting that the initial SEI formation process is similar at silicon and graphite. As the irreversible capacity loss of the first cycle, which is commonly associated with SEI formation, is proportional to the BET surface area of the active material, the amount of SEI loss per delivered capacity, and thus the coulombic efficiency, must consequently be the similar for all compositions.[42] Thus, contrary to common perception, the first cycle coulombic efficiencies of silicon and graphite are actually quite similar in this case. As a corollary, for silicon particles with a lower BET area (i.e., with a lower m^2_{BET} Ah^{-1} value), one would expect them to exhibit equal or even superior coulombic efficiency compared to graphite, as the first-cycle coulombic efficiency seems to scale with m^2_{BET} Ah^{-1} value. Consistent with this assumption, Yoon et al. recently reported a coulombic efficiency of ∼91.5% for silicon particles with a diameter of 700 nm, which is higher than that of graphite.[30]

Within the first 60 cycles, all electrodes reveal a distinct capacity decay (see Figure 2b), which occurs earlier and increases in extent with increasing silicon content. Here we would like to note that this loss of reversible capacity is not related to the depletion of FEC as described by Jung et al.,[11] because our ^{19}F-NMR analysis after 120 cycles revealed a residual FEC concentration of at least ∼1.2 wt% in the electrolyte (originally 5 wt%). The cycling stability notably improves after the initial capacity decays, leading to similar capacity fading rates for all compositions. The resulting capacity retentions between the 3rd (i.e., after formation) and the 120th cycle at 0.5 h^{-1} lie between 67% for the 60 wt% silicon electrode and 82% for the 20 wt% silicon electrode (see Table I), meaning that the silicon/graphite ratio displays a trade-off between the initial delithation capacity and subsequent cycling stability. In addition, all electrode compositions show a minimum in the coulombic efficiency around the 20th cycle (see Figure 2a), followed by a gradual increase to values above 99.5%. Like the capacity decay, the minimum coulombic efficiency value at ∼20 cycles decreases with increasing silicon content. At this point we would like to note that the capacity fade in Figure 2b is not related to a depletion of active lithium, i.e. the capacity of the LFP positive electrode after 120 cycles is still large enough to avoid a limitation in cyclable lithium. The same cycling behavior was also obtained in preliminary experiments in half-cells vs. lithium metal.[31]

Irreversible capacity loss upon cycling.—To understand the irreversible processes taking place in the silicon-graphite electrodes at different stages of cycle life, the total irreversible capacity $\sum Q_{irr}$ as a function of the cycle number is shown in Figure 3. Here, $\sum Q_{irr}$ was calculated as described by Equation 1, with $Q_i^{lithiation}$ and $Q_i^{delithiation}$ being the specific lithiation and delithiation capacities in Ah_{irr} g^{-1}_{el}, while the index *i* stands for the respective cycle number.

$$\sum Q_{irr} = \sum_{i}^{120} \left(Q_i^{lithiation} - Q_i^{delithiation} \right) \quad [1]$$

As can be seen in Figure 3, the $\sum Q_{irr}$ evolution of all electrode compositions is characterized by a sigmoidal shape. The first part consists of an initial offset in $\sum Q_{irr}$ of about 0.13–0.27 Ah_{irr} g^{-1}_{el}, corresponding to the first cycle irreversible capacity described in Table I, and subsequent sigmoidal increase in $\sum Q_{irr}$, with a maximum in the slope after ∼20 cycles, whereby the slope increases with increasing silicon content. The second part after about ∼45 cycles, however, is characterized by a less steep and nearly linear growth of $\sum Q_{irr}$ with cycle number. Interestingly, the sigmoidal increase of $\sum Q_{irr}$ within the first ∼45 cycles implies that the irreversible processes go through a maximum after ∼20 cycles, which also corresponds to the minimum in coulombic efficiency in Figure 2a. We

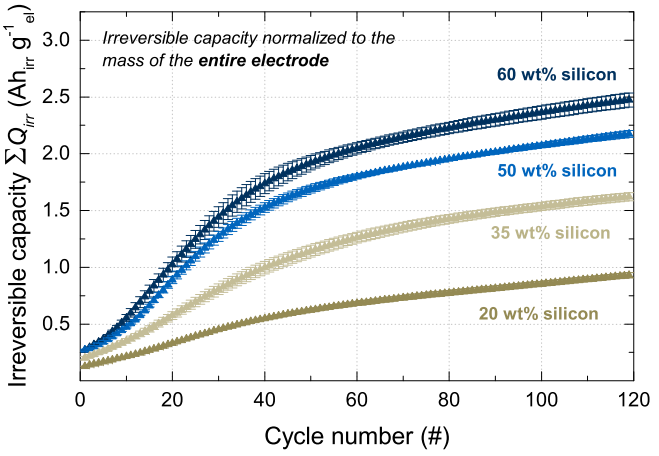

Figure 3. Total irreversible capacity $\sum Q_{irr}$ in units of $Ah_{irr}\ g^{-1}_{el}$ (defined by Equation 1) as a function of the cycle number, obtained from the galvanostatic cycling data of the SiG//LFP coin-cells shown in Figure 2. The error bars represent the standard deviation of at least two independent repeat measurements.

expect that this behavior is caused by the degradation of the silicon particles, which will be explained in more detail in the Discussion section. In contrast to the first phase, the $\sum Q_{irr}$ slopes in the second phase are almost constant and very similar for all electrode compositions (see Figure 3). In this stage, residual irreversible capacity losses are significantly reduced and mainly scale with the delivered capacity, but seem to be independent of the electrode composition.

Silicon-graphite electrode capacity decay.—Figure 4 shows cyclic voltage profiles of the 20 wt% silicon electrode as a function of the exchanged capacity for the 2nd, 20th, 60th, and 120th cycle. For this electrode with the highest graphite content of 65 wt%, the capacity contribution from the graphite active material can be most clearly distinguished from the contributions by silicon. In addition, we plotted the differential capacity curve of the same electrode in Figure 5a, which allows a direct identification of the (de-)lithiation potentials of silicon and graphite (highlighted by hash signs). Accordingly, the cyclic voltage profiles in Figure 4 are increasingly compressed in x-direction upon continued cycling, reflecting a decrease in the reversible capacity of the silicon-graphite electrode. To identify the origin of this capacity decay, we first consider that the delithiation capacity contribution in Figure 4 at potentials below 0.25 V vs. Li/Li^+ stays constant at about 250 mAh g^{-1}_{el}. Taking into account the graphite delithiation potentials obtained from cyclic voltammetry in Figure 1 and the theoretical capacity contribution of ~25% from graphite in the 20 wt% silicon electrode (~75% of the total theoretical capacity of 960 mAh g^{-1}_{el} are contributed by silicon; see Table I), we can conclude that the loss of reversible capacity is mainly associated with the silicon active material at delithiation potentials above 0.25 V vs. Li/Li^+. This conclusion is additionally confirmed by the differential capacity curve shown in Figure 5a, which clearly shows that the integral of the peaks associated with the delithiation from graphite (see hash signs) remain almost constant.

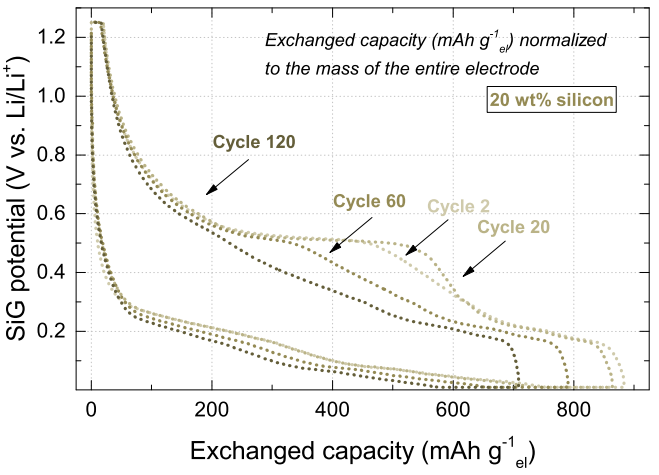

Figure 4. Cyclic voltage profiles of the 20 wt% silicon electrode plotted as a function of the exchanged capacity (mAh g^{-1}_{el}), obtained from galvanostatic cycling of SiG//LFP coin-cells. The SiG electrode potential was calculated from the SiG//LFP cell voltage, referring to a constant LFP electrode potential of 3.45 V vs. Li/Li^+.

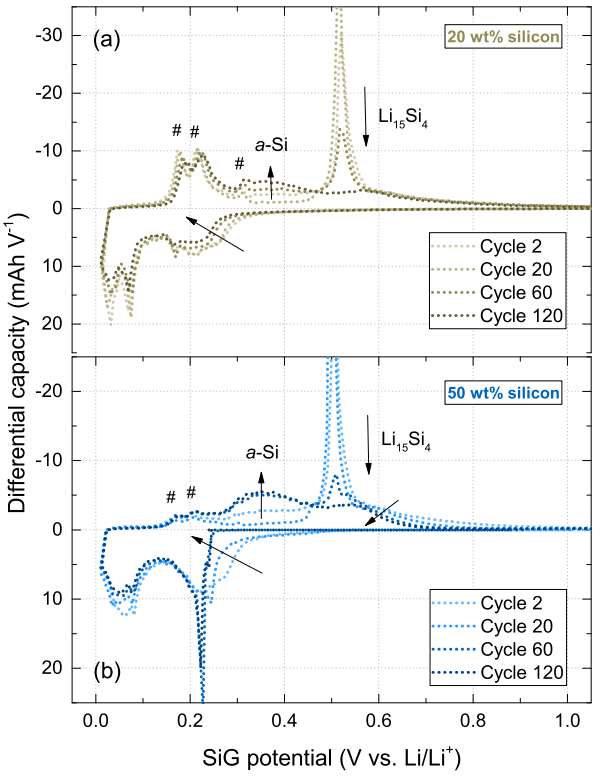

Figure 5. Differential capacity curves of the (a) 20 wt% silicon electrode and (b) 50 wt% silicon electrode plotted as a function of the silicon graphite potential (V vs. Li/Li^+). The data were obtained from galvanostatic cycling of SiG//LFP coin-cells. The SiG electrode potential was calculated from the SiG//LFP cell voltage, referring to a constant LFP electrode potential of 3.45 V vs. Li/Li^+.

In addition, Figure 5b shows the differential capacity profile of the 50 wt% silicon electrode for the 2nd, 20th, 60th, and 120th cycle as a function of the silicon-graphite potential. Both electrodes reveal almost no polarization during the lithiation at potentials below 0.2 V vs. Li/Li^+ upon cycling, however, a distinct potential drop after 60 cycles for the 50 wt% silicon electrode can be observed at low degrees of lithiation, i.e., at potentials above 0.2 V vs. Li/Li^+. As a result, the loss of reversible capacity must be largely caused by an incomplete lithiation of the silicon active material, which can be clearly seen by the disappearance of the lithiation shoulder in the 0.25-0.5 V vs. Li/Li^+ region. Analogously, during delithiation both electrodes reveal significant changes at potentials above 0.25 V vs. Li/Li^+ upon cycling. Between the 2nd and the 20th cycle, a distinct peak at about 0.45 V vs. Li/Li^+ can be seen, which is ascribed to the two-phase delithiation reaction from crystalline $Li_{15}Si_4$ to amorphous $Li_{\sim 2}Si$.[43] As expected, the extent of this peak is larger in the 50 wt% electrode. Several studies on different alloy electrodes indicated that these two-phase boundaries cause additional particle damage due to inhomogeneous volume changes compared

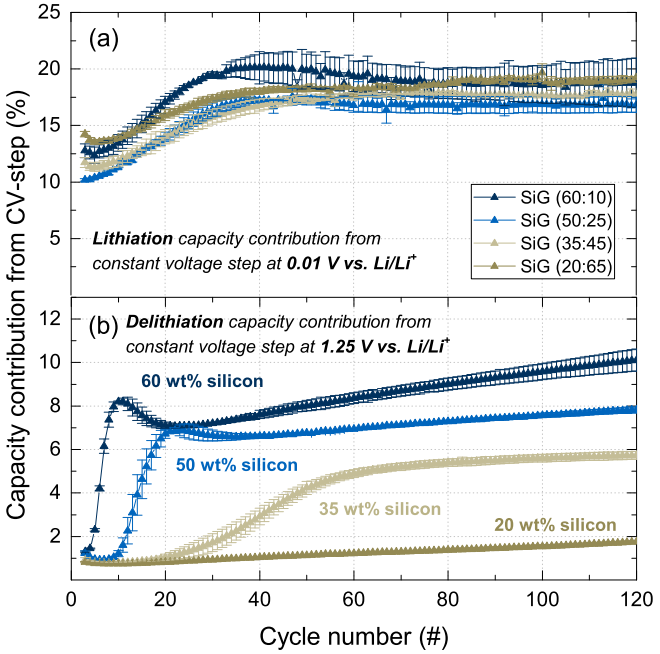

Figure 6. Capacity contribution (in %) from constant voltage steps at the end of (a) lithiation at 0.01 V vs. Li/Li$^+$ and (b) delithiation at 1.25 V vs. Li/Li$^+$, obtained from galvanostatic cycling at 0.5 h^{-1} of SiG//LFP coin-cells shown in Figure 2. The first two cycles were omitted to exclude any effects that may result from the lower C-rate of 0.05 h^{-1} during the first cycle. The error bars represent the standard deviation of at least two independent repeat measurements.

to single-phase reactions and that they often coincide with a capacity fade of the respective electrodes.[7,44] For silicon-based electrodes, Iaboni and Obrovac demonstrated recently that the formation of $Li_{15}Si_4$ during cycling can be used as a sensitive indicator for weakly bound silicon regions and coincides with the detachment of silicon particles, leading to a capacity decay.[6] In agreement with their report, the extent of the $Li_{15}Si_4$ peak shown in Figure 5 increases within the first 20 cycles, which corresponds to a simultaneous decrease of the delithiation from amorphous silicon-lithium alloy (*a*-Si). In other words, during lithiation within the first cycles more silicon is reduced to form the highly lithiated crystalline $Li_{15}Si_4$ phase. However, analogous to the cycling data shown in Figure 2b after 60 cycles a continuous decrease of the $Li_{15}Si_4$ peak can be observed, which, though it is partially compensated by a smaller increase of the delithiation capacity from amorphous silicon-lithium alloy (*a*-Si), indicates that the silicon particles no longer reach the highly crystalline $Li_{3.75}Si$ stoichiometry. Although this effect is more pronounced in electrodes with higher silicon content and can be explained by an incomplete lithiation, the decay of the delithiation capacity at potentials above 0.6 V vs. Li/Li$^+$, i.e. at low degrees of lithiation, is even more severe and the main source for the loss of reversible capacity, which agrees with the disappearance of the shoulder during lithiation at potentials between 0.25 and 0.5 V vs. Li/Li$^+$. This phenomenon is most likely caused by insufficiently connected silicon particles, which suffer either from incomplete lithiation or, more likely, incomplete delithation because of a higher contact and interfacial resistance during particle shrinkage.[30]

Figure 6 shows the capacity contributions $Q_{CV,\%}$ from the constant voltage steps at the end of (a) the lithiation step at 0.01 V vs. Li/Li$^+$ and (b) the delithiation step at 1.25 V vs. Li/Li$^+$ for the different electrode compositions. The contributions for each cycle were calculated according to Equation 2,

$$Q_{CV,\%} = \frac{Q_{CV}}{Q_{CC} + Q_{CV}} \cdot 100 \qquad [2]$$

where Q_{CC} is the capacity from the constant current step and Q_{CV} is the capacity from the constant voltage step. As can be seen in Figure 6a, the lithiation of the silicon-graphite electrodes is characterized by a continuous increase of $Q_{CV,\%}$ by ~6%-points before stabilizing between 17–19% across all electrode compositions. In other words, after ~45 cycles approximately one fifth of the lithiation capacity is derived from the constant voltage step at 0.01 V vs. Li/Li$^+$. The slope of $Q_{CV\%}$ vs. cycle number reaches a maximum after ~20 cycles before it decreases to essentially zero after about ~45 cycles. The occurrence of this inflection point seems to be independent of the electrode composition and again coincides with the minimum in the coulombic efficiency in Figure 2a. We assume that the initial rise in $Q_{CV,\%}$ results from a minor increase in electrode polarization (as shown in Figure 5, the voltage polarization increase for the lithiation process is rather small), which we believe originates from enhanced electrolyte decomposition in the initial cycles due to silicon particle degradation (i.e., surface growth) and subsequent growth of the SEI layer. Upon continued cycling (i.e., after ~45 cycles), the increase in $Q_{CV,\%}$ is only minor across all electrode compositions. As it is known that the SEI layer mainly consists of electrically insulating electrolyte decompositions products, e.g., inorganic LiF and Li_2CO_3 compounds as well as organic alkyl carbonates and alkoxides, its growth is limited to a certain thickness.[45,46] Hence, we expect that the silicon surface does not change significantly after cycle 45.

As the electrode polarization during lithiation does not seem to depend on the electrode composition, there must exist a second degradation phenomenon during delithiation that leads to the observed composition-dependent capacity drop shown in Figure 2. To further investigate this, the capacity contribution from the CV-step at 1.25 V vs. Li/Li$^+$ during delithiation is shown Figure 6b. Initially, $Q_{CV,\%}$ is in the range of ~1% across all electrode compositions and thus much smaller compared to that of the lithiation CV step. This can be explained by considering exemplarily the differential capacity curves in Figure 5, according to which the delithiation cutoff potential of all silicon-graphite electrodes, independent of the silicon content, is significantly higher than the average delithiation potential of ~0.5 V vs. Li/Li$^+$. However, for the silicon-rich SiG electrode with 60 wt% silicon, $Q_{CV,\%}$ rises rapidly after the first cycle, reaching ~8% within less than 10 cycles, which indicates an increased difficulty to completely delithiate the silicon particles. The same is observed for the 50 wt% and the 35 wt% SiG electrodes, which display a sharp increase of the $Q_{CV,\%}$ value after ~10 and ~20 cycles, respectively. While also for the Si-poor SiG electrode with 20 wt% silicon a gradual increase of $Q_{CV,\%}$ is observed after ~30 cycles, the magnitude of this increase is substantially smaller than for the electrodes with higher silicon content. In summary, the higher the silicon content of the SiG electrodes, the earlier initiates the observed increase in $Q_{CV,\%}$ and the higher is the magnitude of the $Q_{CV,\%}$ increase. Remarkably, the onset and the extent of the increase of $Q_{CV,\%}$ during the delithiation cycles shown in Figure 6b coincides with the onset and the extent of the distinct capacity decay within the first 60 cycles as shown in Figure 2. The origin of this phenomenon will be further examined in the Discussion section.

Electrolyte consumption.—Besides the capacity decay, continuous consumption of the electrolyte constitutes a severe challenge to silicon-based electrodes. To quantify the loss of electrolyte caused by side reactions at the silicon/electrolyte interface, we harvested the electrolyte-soaked separators from the cycled SiG//LFP coin-cells after 120 cycles and measured ^{19}F-NMR of the extracted electrolytes. As FEC is reduced at more positive potentials than EC or EMC, Jung et al. demonstrated by on-line electrochemical mass spectrometry (OEMS) that FEC almost entirely suppresses the decomposition of EC as long there is FEC present in the electrolyte.[11] Hence, we consider in the following the change in the ratio of the FEC and PF_6^- peak integrals as a sensitive indicator for the electrolyte consumption upon cycling.

Figure 7a shows the total charge+discharge capacity per mole of FEC obtained from the SiG//LFP coin-cells depicted in Figure 2 after 120 cycles. This consumption rate was calculated by Equation 3,

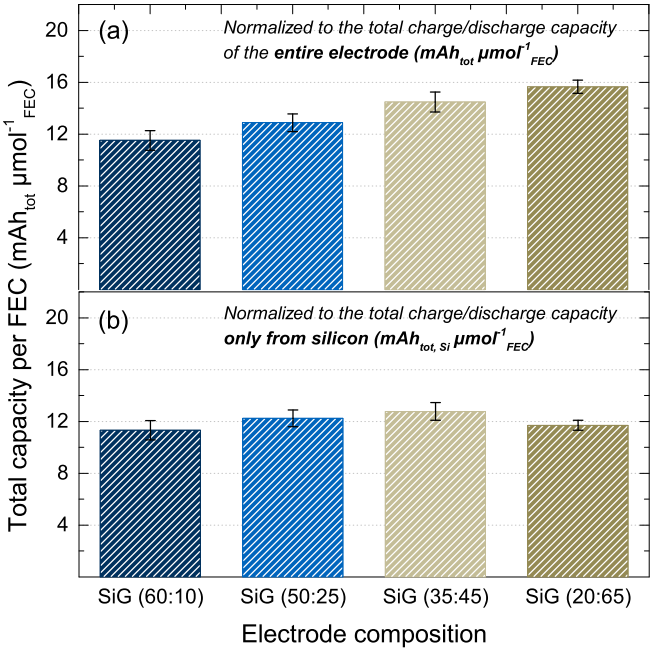

Figure 7. Total charge+discharge capacity (as defined by Equation 4) per mole of FEC after 120 cycles, using the cycling procedure described in Figure 2. The consumed amount of FEC was determined by ^{19}F-NMR spectroscopy from electrolytes that were harvested from SiG//LFP coin-cells after 120 cycles. (a) Total capacity of the entire electrode (mAh$_{tot}$ µmol$^{-1}_{FEC}$), (b) Total capacity contributed only from the silicon active material (mAh$_{tot, Si}$ µmol$^{-1}_{FEC}$). The error bars represent the standard deviation of at least two independent repeat measurements.

where $\sum Q_{tot}$ is the total charge exchanged during charging and discharging in mAh$_{tot}$ (see Equation 4) and n_{FEC} is the FEC consumption in µmol$_{FEC}$ as determined from integral analysis of the ^{19}F-NMR spectra. In other words, this thus determined capacity per FEC describes the amount of charge that can be exchanged by the silicon active material until 1 µmol of FEC is consumed by concomitant side reactions.

$$Capacity\ per\ FEC = \frac{\sum Q_{tot}}{n_{FEC}} \quad [3]$$

$$\sum Q_{tot} = \sum_{i}^{120} \left(Q_i^{lithiation} + Q_i^{delithiation}\right) \quad [4]$$

As can be seen, the total capacity per mole of FEC increases gradually with decreasing silicon content from 11.5 mAh$_{tot}$ µmol$^{-1}_{FEC}$ in the 60 wt% silicon electrode to 15.7 mAh$_{tot}$ µmol$^{-1}_{FEC}$ in the 20 wt% silicon electrode. Taking into account a density of 1.41 g cm^{-3} for FEC, this would correspond to a total capacity per µL FEC of 150–210 mAh$_{tot}$ µL$^{-1}_{FEC}$. Interestingly, this difference is comparatively small, especially when considering that the 60 wt% silicon electrode contains nominally three times more silicon compared to the 20 wt% silicon electrode. For that reason, we applied Equation 5 to correct the total exchanged capacity by the capacity contribution from graphite to obtain the capacity that results only from the (de-)lithiation of silicon (mAh$_{tot, Si}$ µmol$^{-1}_{FEC}$) as shown in Figure 7b,

$$\sum Q_{tot,\ Si} = \sum Q_{tot} \cdot \frac{x_{Si} \cdot Q_{Si}^{theo}}{x_{Si} \cdot Q_{Si}^{theo} + x_C \cdot Q_C^{theo}} \quad [5]$$

where $\sum Q_{tot,Si}$ is the total capacity from silicon, $\sum Q_{tot}$ is the total capacity from the entire electrode (see 1st and 2nd rows in Table I), Q_{Si}^{theo} is the theoretical capacity of silicon, Q_C^{theo} is the theoretical capacity of graphite, x_{Si} is the relative amount of silicon, and x_C is the relative amount of graphite. It is to note that for reasons of simplicity, we make the approximation that the ratio of the capacity contributions of silicon and graphite remains constant throughout cycling. As the silicon accounts for the majority of the capacity (>75%) in any case, the error arising from this assumption should be low, even if the capacity of graphite and silicon in the SiG electrodes would fade at different rates. Using Equation 5 to quantify the charge+discharge capacity contribution from silicon and dividing its value by the measured FEC consumption, it can be seen in Figure 7b that the thus calculated total capacity from silicon per mole of FEC falls within a very narrow range, with mean values for each SiG electrode composition which differ from each other by less than one standard deviation, so that the overall capacity per consumed FEC can be averaged for all four SiG electrode compositions to 12.0 ± 0.8 mAh$_{tot, Si}$ µmol$^{-1}_{FEC}$. From this, we conclude that the total capacity exchanged by silicon causes the same FEC consumption across all SiG electrode compositions, suggesting that the graphite content has no influence on the FEC consumption rate.

$$FEC\ per\ irreversible\ capacity = \frac{n_{FEC}}{\sum Q_{irr}} \quad [6]$$

$$Electrons\ per\ FEC = \frac{\sum Q_{irr}}{n_{FEC} \cdot F} \quad [7]$$

To further support our conclusion, we applied Equation 6 to normalize the FEC consumption n_{FEC} after 120 cycles to the total irreversible capacity $\sum Q_{irr}$ (see Equation 1). As a result of the repeated volume expansion of silicon (~280%) and the resulting cracking and continuous renewal of the SEI layer, we assume that the irreversible capacity losses after 120 cycles can be almost fully ascribed to the side reactions at the silicon/electrolyte interface. In accordance with that, the normalization reveals a similar ratio of 11.5-13.1 µmol$_{FEC}$ mAh$^{-1}_{irr}$ across all electrode compositions (shown in Table I), which is in good agreement with the results obtained by Jung et al. and additionally confirms their hypothesis according to which there is only one major source of irreversible capacity loss on silicon when using FEC containing electrolytes, namely the reduction of FEC.[11] However, by use of Equation 7, the conversion of the µmol$_{FEC}$ mAh$^{-1}_{irr}$ into the number of electrons that are consumed by the reduction of FEC reveals a slightly lower value of 3.0 ± 0.2 compared to the proposed four-electron mechanism of Jung et al.[11] We ascribe this discrepancy to the influence of the two constant voltage steps at 0.01 and 1.25 V vs. Li/Li$^+$ in the present study, as result of which our silicon-graphite electrodes experienced these limiting potentials for a much longer time compared to the constant current procedure of Jung et al.,[11] which in turn seem to affect the reduction processes at the silicon/electrolyte interface.

Building up on the relation of the FEC consumption and the irreversible capacity of 11.5–13.1 µmol$_{FEC}$ mAh$_{irr}$, we can now compare the silicon-graphite electrodes with a standard graphite:PVdF (95:5) electrode with the same graphite particles in a conventional graphite//LFP full-cell cycling procedure (~1.7 mAh cm^{-2}, CCCV cycling between 2.0–4.0 V at 1 C), which shows a total irreversible capacity of ~0.34 mAh per 550 mAh total charge-discharge capacity (after ~200 cycles). By multiplying the total irreversible capacity with the FEC consumption rate (here: 13.1 µmol$_{FEC}$ mAh$_{irr}$), we obtain an absolute FEC consumption of 4.45 µmol$_{FEC}$ (see Equation 6). Subsequent normalization of the total charge-discharge capacity of 550 mAh to the absolute FEC consumption in accordance with Equation 3 results in a total capacity per FEC of ~124 mAh µmol$_{FEC}$. Comparing this value to the capacities per FEC for the different silicon-graphite electrodes of 11.5–15.7 mAh µmol$_{FEC}$ (see Figure 7a) clearly shows that the FEC consumption caused by the (de-)lithiation of graphite is more than one order of magnitude smaller as for silicon and likely mainly results from the initial SEI formation during the first cycles.

Discussion

Differentiating the degradation phenomena in silicon-graphite electrodes.—A close inspection of the galvanostatic cycling data

(Figure 2) and the two different regions in the corresponding total irreversible capacity vs. cycle number plot (Figure 3) suggest that our silicon-graphite electrodes undergo two distinct degradation phenomena. There seems to be one degradation mechanism common to all SiG electrodes, which results in an initial dip in the coulombic efficiency over the first ∼45 cycles, which goes through a minimum after ∼20 cycles (see Figure 2a), and which results in a rapid initial increase in the CV-step lithiation capacity (see Figure 6a). Although the extent of the coulombic efficiency minimum increases with the silicon content in the electrodes, it occurs after the same number of charge/discharge cycles across all electrode compositions, independent of the silicon/graphite active material ratio. In contrast, there seems to be another degradation mechanism which depends on the silicon/graphite ratio, namely the initially rapid and distinct capacity decay (see Figure 2b) as well as the clearly different increase in the delithiation capacity during the CV-step (see Figure 6b). As will be outlined in the following, we propose that the first phenomenon is mostly related to the intrinsic properties of the silicon active material such as particle size and morphology (furtheron referred to as *silicon particle degradation*), whereas the second phenomenon depends not only on the silicon material but also on the electrode composition, viz., the silicon/graphite ratio (furtheron described as *electrode degradation*).

Our hypothesis that the first degradation mechanisms, i.e., the silicon particle degradation mechanism indeed mostly depends on the intrinsic properties of the silicon particles can be illustrated by normalizing the accumulated irreversible capacity $\sum Q_{irr}$ (in $Ah_{irr}\ g^{-1}{}_{el}$) shown in Figure 3 by the silicon content of the respective silicon-graphite electrodes and plotting the resulting $\sum Q_{irr,Si}$ (in $Ah_{irr}\ g^{-1}{}_{Si}$) as a function of the cycle number, as shown in Figure 8a, as well as a function of the total charge-discharge capacity (see Figure 8b). The most important finding of this analysis is that all four SiG electrode compositions now show an essentially identical behavior, thus revealing that the total irreversible capacity only depends on the amount of silicon in the electrodes, with apparently negligible contributions from the silicon/graphite ratio or from the graphite content. Furthermore, by plotting $\sum Q_{irr,Si}$ versus the total amount of exchanged charge (see Equation 4), Figure 8b shows that $\sum Q_{irr,Si}$ is identical for all SiG electrodes, consistent with the observation that the FEC consumption of all SiG electrodes only depends on the total charge+discharge capacity (see Figure 7b).

To explain the initial sigmoidal increase of the accumulated irreversible capacity losses ($\sum Q_{irr}$), we consider that alloy electrode materials suffer from an enhanced particle roughening and from the formation of nanoporous particle morphologies as a consequence of the repeated volume changes during lithiation/delithiation, as was reported for tin[7] and silicon[10] (analogous to the structures formed during dealloying reactions).[47] Assuming that nanoporous silicon particles are being created during the early phase of the charge/discharge cycling, the sigmoidal behavior of the accumulated irreversible capacity versus cycle number (see Figure 8a) can easily be rationalized: the associated rapid initial increase in silicon particle surface area would lead to an initial steep increase in the accumulated irreversible capacity due to enhanced SEI formation, which subsequently would slow down once a fully developed nanoporous particle morphology has been reached. As this phenomenon would only depend on the silicon particle size and morphology, its effect would have to be independent of the silicon/graphite ratio of the SiG electrodes, as long as the electrodes are cycled between identical potential limits (i.e., between identical degrees of silicon lithiation/delithation), as indeed is observed in Figure 8. Furthermore, this hypothesis is consistent with the fact that the characteristic dip in the coulombic efficiency with a minimum after the same number of cycles is the same for all SiG electrode compositions, independent of the silicon/graphite ratio (see Figure 2a).

As can be seen in Figure 8, the silicon particle degradation is significantly decreased after ∼ 45 cycles, leading to a much reduced slope of the accumlated irreversible capacity versus cycle number or total exchanged charge. This would be consistent with the assumption

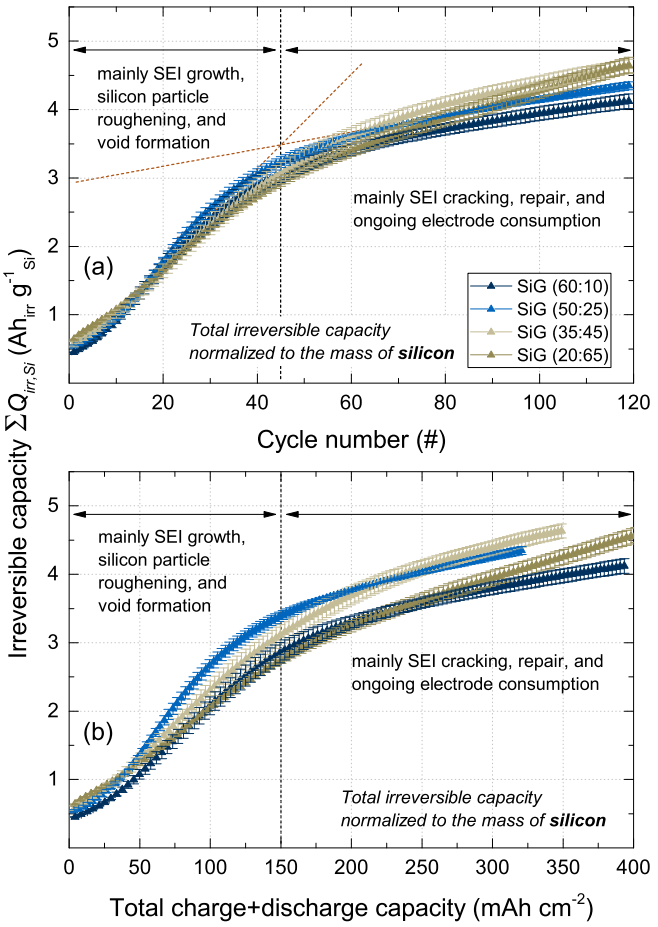

Figure 8. Total irreversible capacity $\sum Q_{irr,Si}$ ($mAh_{irr}\ g^{-1}{}_{Si}$) normalized to the mass of silicon in the SiG electrodes compositions (same color codes as in Figure 3) and plotted (a) as a function of the cycle number, and (b) as a function of the total charge+discharge capacity. The data were obtained from galvanostatic cycling of SiG//LFP coin-cells, as shown in Figure 2.

that a steady-state morphology of the silicon particles is reached after the initial ∼45 cycles, i.e., that the silicon surface area has reached a final steady-state value. We explain this behavior by a reduction of the mechanical stress during insertion and extraction of lithium in the nano-sized silicon features, resulting from the initial morphological changes. In addition, this may also be related to the fact that the hypothesized increased surface area and porosity of the silicon particles would lead to a decrease of the effective surface-normalized current density, which in turn would reduce the mechanical stresses due to volume changes during cycling. In other words, the degradation of the silicon particles results in morphological changes that simultaneously diminish the root cause for their mechanical degradation, namely the mechanical stress upon insertion and extraction of lithium.[22] Once the surface growth of silicon has reached a minimum and the silicon particles are fully covered by an electronically insulating SEI layer, further irreversible capacity losses at a now much lower rate would mainly originate from ongoing electrolyte decomposition due to cracking and repair of the existing SEI layer, which is caused by the repeated volume changes upon cycling.

While the here given hypothesis is consistent with the literature, we are currently seeking to provide microscopic proof for the proposed relationship between nanoporous particle formation and the behavior of the accumulated irreversible capacity versus cycle number.[48]

In contrast to the silicon particle degradation mechanism, the electrode degradation mechanism is highly dependent on the electrode composition, with an observed earlier (in terms of cycle number) and more severe decay of the reversible capacity with increasing silicon

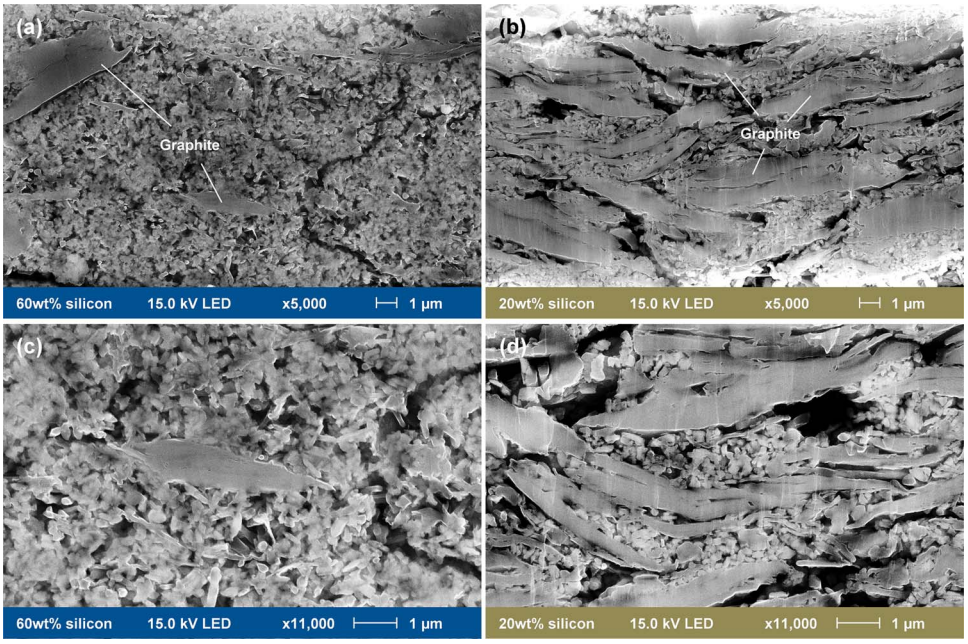

Figure 9. Scanning electron microscope cross-sectional images of (a, c) the 60 wt% silicon electrode, and (b, d) the 20 wt% silicon electrode. Secondary electron detector (SE), 15.0 kV electron acceleration voltage, magnification x5,000 (upper panels) and x11,000 (lower panels). Cross-sections were prepared with an Ar-ion beam cross-section polisher.

content as shown in Figure 2b. Similarly, the delithiation capacity contribution of the CV-step at 1.25 V vs. Li/Li$^+$ in Figure 6b strongly increases with increasing silicon content, indicating an increasingly significant polarization of the delithiation reaction of the silicon particles. To understand how the electrode composition might lead to these observations, Figure 9 shows representative cross-sectional scanning electron microscope (SEM) images of (a, c) the 60 wt% silicon electrode and (b, d) the 20 wt% silicon electrode. The lower SEM images (c, d) depict magnifications of the upper electrodes (a, b) at 11,000x. As can be seen in (a) and (c), the 60 wt% silicon electrode consists of a dense matrix of nanometer-sized silicon particles into which a few graphite flake-like particles are widely dispersed. Therefore, electronic conduction through this silicon-rich electrode involves the contribution of a large number of silicon/silicon and silicon/carbon fiber contact junctions, with the associated electronic contact resistances. In contrast, the 20 wt% silicon electrode in (b) and (d) consists of a nearly contiguous graphite backbone structure, whose interspaces are partially filled by silicon particles, leading to a much smaller average distance between the individual silicon particles and adjacent graphite particles. Therefore, the electronic conductivity of the SiG electrodes is expected to be significantly improved with increasing graphite content.

Although the SEI growth is largely driven by the above described silicon particle degradation mechanism, the mean electron conduction path length from the individual silicon particles to the graphite particles is crucial to maintain sufficient electronic conductivity throughout the electrode, which we tried to capture by Scheme 2. Based on this, one would expect that the progressive surface roughening of the silicon particles in the early stages of SEI growth would lead to a substantial loss of electrode integrity and subsequent increase of the electrode resistance. This, however, seems to be only partially consistent with the analysis of the potential profiles (see Figure 5) over extended charge/discharge cycling: while the gradual disappearance of the $Li_{15}Si_4$ phase is consistent with an electronic conduction resistance induced electrode polarization, the observed overpotential increase during charge and discharge is rather small and there are no obvious differences between the different SiG composites. On the other hand, our hypothesis of increased local electronic resistance contributions with increasing silicon content seems to hold when examining the capacity contribution during the delithiation CV step (at 1.25 V vs. Li/Li$^+$, see Figure 6b), which rapidly rises for silicon-rich electrodes in contrast to SiG electrodes with low silicon content. This can be easily explained by the silicon particle shrinkage during delithiation, resulting in a temporary particle isolation and incomplete delithiation, as was shown previously by Yoon et al.[30] Consistent with this hypothesis is the observation that the capacity contribution during the lithiation CV step (at 0.01 V vs. Li/Li$^+$, see Figure 6a) is similar for all SiG composites, as the expanded volume of the lithiated silicon particles will reduce the effect of inter-particle electronic contact resistances. The fact that the electrode polarization effects only set in toward the end of the delithiation process now also explains why it is not apparent in the overall differential capacity curves (Figure 5). In summary, we believe that the increasing capacity decay rate with increasing silicon content is due to silicon particle detachment and loss of electrical contact, particularly during the delithiation step, caused by the increasingly long mean electron conduction

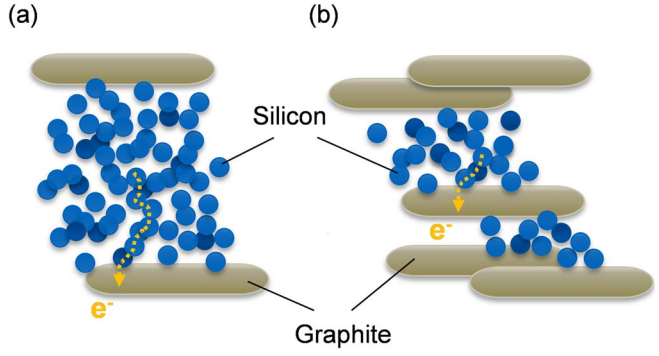

Scheme 2. Illustration of the difference in the mean electron conduction path length from the individual silicon particles to the electronically conductive graphite particles as a function of the silicon/graphite ratio sketched for (a) an Si-rich electrode (based on Figures 9a and 9c) and (b) an Si-poor electrode (based on Figures 9b and 9d). The different path lengths for electron conduction are illustrated by the yellow dotted line.

path length with increasing silicon content (see Scheme 2). Thus, in contrast to the silicon particle degradation mechanism, the electrode degradation mechanism and the concomitant capacity decay of the SiG electrodes is largely determined by the silicon/graphite active material ratio.

To estimate the contribution from the incomplete delithiation to the total irreversible capacity, we first considered that the loss of reversible capacity of the 60 wt% silicon electrode between the 3rd and the 120th cycle accounted for 634 mAh g^{-1}_{el} (see Figure 2b). Taking into account that the incomplete delithiation mainly affects silicon particles at low degrees of lithiation, i.e., below roughly 25% state-of-charge (compare Figure 5b), the maximum amount of immobilized lithium in these particles is 159 mAh g^{-1}_{el} (= 0.25 × 634 mAh g^{-1}_{el}). Comparing this number to the total irreversible capacity of 2.47 Ah g^{-1}_{el} after 120 cycles shown in Figure 3 yields a contribution of less than ∼6.4%. With decreasing silicon content and improved electrical conductivity within the electrodes (compare Figure 6b) this value is expected to decrease further. As a result, despite its harmful impact on the reversible capacity, the irreversible capacity caused by incomplete delithiation of the silicon particles displays only a minor contribution compared to irreversible capacity caused by the continuous electrolyte decomposition at the silicon/electrolyte interface.

Estimation of the electrode pore clogging upon cycling.—The sheer extent of the electrolyte consumption shown in Figure 7 suggests that the SEI on silicon is less a conformal surface layer formed in the initial cycles that evenly surrounds the silicon particles, but instead an increasingly thick and electrically insulating matrix (see above discussion and Figure 6b) that penetrates the entire porous electrode structure. For that reason, we decided to modify the approach of calculating the number of monolayers that are formed on the electrode's surface, which was recently reported by Jung et al.[11] and Pritzl et al.,[49] and characterize the electrolyte decomposition products by an average density rather than an average area defined by a C-C single bond length and thus also take into account the reduction of previously evolved CO_2 gas. To quantify how much SEI volume the SiG electrodes could accommodate before being entirely clogged by electrolyte decomposition products, we will present in the following an estimate of the relative SEI volume after 120 cycles and compare it to the pore volume of the pristine electrodes. Starting from the electrode properties shown in Table I, we first calculate the absolute pore volumes V_{pore} of the different electrode compositions, according to Equation 8,

$$V_{pore} = d \cdot A \cdot \varepsilon \quad [8]$$

where d is the pristine electrode thickness (see Table I), A is the electrode area (1.54 cm^2), and ε is the electrode porosity (see Table I). As can be seen from Table II, the resulting pore volumes increase with decreasing silicon content from 1.54 μL (∼1.00 μL cm^{-2}) for the 60 wt% electrode to 3.26 μL (2.21 μL cm^{-2}) for the 20 wt% silicon electrode, due to the increase of the electrode thickness from ∼15 to ∼30 μm at nearly similar electrode porosities (∼67–73%, see Table I).

In the next step, we approximate the mass of the SEI m_{SEI} from Equation 9 by taking into account the FEC consumption n_{FEC} determined by post-mortem ^{19}F-NMR analysis. Herein, we assume that the SEI has an equivalent mass as the preceding FEC decomposition product m_{FEC*}. In addition, we correct the molar mass of FEC (M_{FEC} = 106.05 g mol^{-1}) by the molar mass of four lithium atoms (M_{Li} = 6.84 g mol^{-1}) that are also incorporated into the SEI compounds (e.g., LiF or Li_2O),[11] leading to an effective molar mass M_{FEC*} of the FEC decomposition product of 133.41 g mol^{-1}.

$$m_{SEI} \equiv m_{FEC^*} = n_{FEC} \cdot M_{FEC^*} \quad [9]$$

Building up on this, we can further calculate the SEI volume V_{SEI}, as described by Equation 10, thereby assuming an average density ρ_{SEI} of 1.4–1.8 g cm^{-3} for the SEI. This value is a very rough zero order estimate based on the densities of the different SEI compounds, including ∼50% of inorganic compounds, inter alia LiF (2.64 g cm^{-3}), Li_2CO_3 (2.11 g cm^{-3}), Li_2O (2.01 g cm^{-3}), and ∼50% organic compounds, such as lithium alkoxides (∼1.0 g cm^{-3}), which are typically observed via for cycled silicon electrodes in FEC-containing electrolyte by XPS spectroscopy.[50–52]

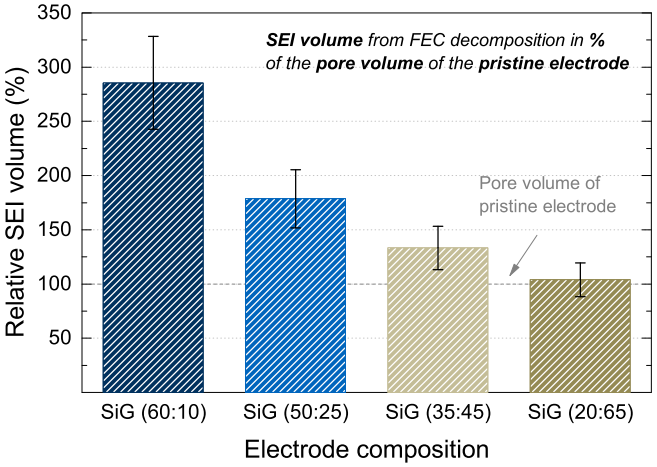

Figure 10. Estimated relative SEI volume defined by the fraction of pore volume of the pristine silicon-graphite electrodes which is occupied by FEC decompositions products. The values were calculated from a zero-order estimate based on the FEC consumption from ^{19}F-NMR. The SEI volume was calculated based on an average density of 1.6 g cm^{-3} for the FEC decomposition products. The error bars represent a variation in the density between 1.4–1.8 g cm^{-3}.

$$V_{SEI} = \frac{m_{SEI}}{\rho_{SEI}} \quad [10]$$

Finally, we divide the SEI volume V_{SEI} by the pore volume V_{pore} of the pristine electrodes by using Equation 11 to obtain the relative SEI volume v_{SEI}, which gives us an impression of the fraction of the original pore volume that would be occupied by electrolyte decomposition products after 120 cycles.

$$v_{SEI} = \frac{V_{SEI}}{V_{pore}} \quad [11]$$

Figure 10 shows the resulting zero order estimates of the relative SEI volumes normalized to the pore volume of the pristine electrodes. While this very simple approximation does not include the swelling of the electrodes over the course of cycling, it nonetheless provides a semi-quantitative measure of the volume of the electrolyte decomposition products and how it compares to the initially available void volume of the SiG electrodes. A comparison of the different electrode compositions in Figure 10 reveals a strong dependence of the relative SEI volume after 120 cycles on the silicon/graphite ratio, decreasing with decreasing silicon content from ∼280% to ∼100%. This grantedly simple estimate provides a reasonably convincing argument that the FEC decomposition products after 120 cycles would have to lead to an essentially complete pore blocking in the case of the 20 wt% silicon electrode and could not even be accommodated in the 60 wt% silicon electrode. Therefore, considering that about three quarters of the accumulated irreversible capacity occur within the first ∼45 cycles (see Figure 8a), and given that the SEI formation is proportional to irreversible capacity, we can assume that without any changes in electrode morphology and thickness, all ionic pathways would be filled by electrolyte decomposition products after less than 45 cycles. However, as our results from galvanostatic cycling clearly prove a residual reversible capacity of ∼70% after 120 cycles for the 60 wt% silicon electrode (see Figure 2), we conclude that the electrodes must significantly swell upon cycling in order to increase the available pore volume and thus facilitate the accommodation of the FEC decomposition products while simultaneously conserving the ionic conduction pathways. These conclusions agree well with the thickness

Table II. Pore volumes of the pristine electrodes and calculated SEI volumes after 120 cycles, based on the FEC consumption after 120 cycles n_{FEC} determined by post-mortem ^{19}F-NMR. The SEI volume was calculated based on an average density of 1.6 g cm^{-3} for the FEC decomposition products.

		Electrode composition			
Measures	Units	SiG (60:10)	SiG (50:25)	SiG (35:45)	SiG (20:65)
Electrode pore volume V_{pore}	µL	1.54	1.79	2.32	3.26
FEC consumption after 120 cycles n_{FEC}	µmol	53	38	37	41
Mass of FEC* precipitates m_{FEC*}	mg	7.1	5.1	4.9	5.4
Absolute SEI volume V_{SEI}	µL	4.4	3.2	3.1	3.4
Relative SEI volume	%	285	179	133	104

measurements and cross-sectional SEM images of cycled silicon electrodes reported by Mazouzi et al.[53]

Obrovac and co-workers measured the coating thickness of Si-alloy/graphite composite electrodes in their fully lithiated state and found that the entire coating expanded by about ∼96%, which was very similar to the expected expansion of the lithiated Si-alloy (∼115%).[15] Interestingly, the porosity of these electrodes remained nearly the same as in the delithiated state, leading them to the conclusion that the pore size expands by the same amount as the silicon particles. Transferring these observations to our electrodes, the silicon particle volume increase of about 280% upon full lithiation would result in an additional pore volume of 60–170% (e.g., 60 wt% silicon x 280% expansion = ∼170% additional pore volume), depending on the electrode composition. As the pores are increasingly filled by decomposition products upon cycling, they likely cannot shrink back to their initial volume when silicon is delithiated. Hence, the electrode thickness will increase continuously, in particular during the silicon particle degradation phase, where electrolyte decomposition and subsequent SEI growth are strongest. In contrast, a higher graphite content of the composite electrodes increases the total pore volume and simultaneously improves the electrode conductivity with graphite acting as an electrically conductive backbone.

Cycle life dependence on the electrolyte amount.—Besides the electrode morphology, the amount of SEI-forming additives in the electrolyte also plays a crucial role for the cycling performance of silicon-based electrodes. Thus it was shown that a rapid capacity drop can be observed for silicon based anodes at the point where the capacity-stabilizing FEC additive was found to be depleted quantitatively.[11,35] As in commercial-scale Li-ion batteries the electrolyte amount is in the order of ∼5 µL cm^{-2} and thus much smaller compared to typical lab-scale measurements (∼85 µL cm^{-2} for our coin cells), the available moles of FEC per mass of silicon are substantially lower in commercial-scale cells, so that the expected cycle life of silicon-based electrodes in commercial-scale cells should consequently be much shorter.[11] To quantify this difference, we approximate the number of cycles prior to FEC depletion of SiG electrodes in lab-scale versus commercial-scale cells by considering the constant ratio of the FEC consumption n_{FEC} and the irreversible capacity loss $\sum Q_{irr}$ (see Table I). Assuming a commercial-scale cell using 5 µL cm^{-2} electrolyte with 20 wt% FEC additive and our lab-scale cells using 85 µL cm^{-2} electrolyte with 5 wt% FEC additive, we use Equation 12 to first determine the absolute amount of FEC n_{FEC}^{tot} in the two electrolytes.

$$n_{FEC}^{tot} = \frac{V_{el} \cdot \rho_{el} \cdot x_{FEC}}{M_{FEC}} \quad [12]$$

where V_{el} is the electrolyte volume, ρ_{el} is the electrolyte density (∼1.19 g cm^{-3}), x_{FEC} is the mass fraction of FEC in the electrolyte, and M_{FEC} is the molar mass of FEC (106.05 g mol^{-1}). Accordingly, the commercial-scale cell would contain ∼11 µmol cm^{-2} of FEC, whereas the lab-scale cells tested in this work contain ∼48 µmol cm^{-2} of FEC, i.e, the ∼5-fold amount. In the next step, we use the inverse of the constant ratio of the FEC consumption n_{FEC} to irreversible capacity loss $\sum Q_{irr}$ (in units of µmol$_{FEC}$ Ah$^{-1}_{irr}$, calculated by Equation 6, shown in Table I) to calculate the maximal irreversible capacity $\sum Q_{irr}^{max}$ that corresponds to a total depletion of FEC from the respective electrolytes, according to Equation 13,

$$\sum Q_{irr}^{\max} = n_{FEC}^{tot} \cdot \frac{\sum Q_{irr}}{n_{FEC}} \cdot \frac{1}{m_{Si}} \quad [13]$$

where m_{Si} is the mass of silicon in the electrode (in mg$_{Si}$ cm^{-2}), and n_{FEC}^{tot} is the total amount of FEC per cm^2 electrode area (µmol$_{FEC}$ cm^{-2}). Table III summarizes the maximal irreversible capacities $\sum Q_{irr}^{max}$ of the various silicon-graphite electrodes in either lab-scale cells or in commercial-scale cells. To forecast the number of cycles until the depletion of FEC, we can compare the accumulated irreversible capacity versus cycle number in Figure 8a with the maximal irreversible capacity until FEC depletion (in units of Ah$_{irr}$ g$^{-1}_{Si}$) listed in Table III for both cell formats. For the commercial-scale cells, this analysis suggests that FEC would already be consumed within the first ∼20–30 charge/discharge cycles. In contrast, the number of cycles prior to FEC depletion predicted for our lab-scale cells substantially exceeds the here tested 120 cycles (at this point, $\Sigma Q_{irr,Si}$ in Figure 8a is still much below the projected estimated maximal irreversible capacity given in Table III). That FEC, as predicted, is not depleted after 120 cycles in our lab-scale experiments is confirmed by our post-mortem ^{19}F-NMR measurements, which show a residual FEC content of >1.2 wt% in the electrolyte (originally 5 wt%) after the 120 cycles.

Thus, we conclude that the lifetime of silicon-graphite electrodes in commercial-scale cells with a reasonably sized positive electrode would be limited by the amount of FEC in the electrolyte, rather than by the degradation of the electrode structure. These findings highlight again the importance of an effective SEI on silicon-based electrodes and the need for a proper quantification of the electrolyte consumption. Therefore, we recommend that future investigations of silicon-based electrodes in lab-scale cells should take into account the actual FEC consumption in µmol$_{FEC}$ and to compare this to the FEC inventory in commercial-scale cells. As our results from ^{19}F-NMR analysis reveal an almost constant ratio of the consumed FEC n_{FEC} to cumulative irreversible capacity $\sum Q_{irr}$ of 11.5-13.1 µmol$_{FEC}$ mAh$^{-1}_{irr}$, Equation 14 can be used as an approximation to assess the FEC consumption from battery cycling. We would like to note that this relation is only valid for cell chemistries that do not have further electrolyte decomposition reactions at the positive electrode, e.g., $LiFePO_4$, and involve two constant voltage steps. If the cycling protocol does not include any constant voltage steps, the ratio r_{FEC} of the consumed FEC n_{FEC} to total irreversible capacity $\sum Q_{irr}$ approaches the four electron reduction mechanism of FEC, which was reported by Jung et al.,[11] corresponding to a value of 9.4 ± 0.4 µmol$_{FEC}$ mAh$^{-1}_{irr}$.[54]

$$n_{FEC} = r_{FEC} \cdot \sum Q_{irr} \quad [14]$$

Conclusions

In this study, we presented a comprehensive approach to understand the degradation phenomena in silicon-graphite electrodes with different graphite/silicon ratios (20–60 wt% silicon) and areal

Table III. Maximal irreversible capacity and forecasted cycle life of silicon-graphite electrodes calculated for typical lab-scale and commercial-scale cells. The upper segments provide the specifications of the various SiG electrodes as well as the measured FEC consumption per accumulated irreversible capacity over 120 cycles (taken from Table I). The middle and the lower segments provide the estimated number of cycles for lab-scale and commercial-scale cells by which the available amount of FEC will be consumed.

		Electrode composition			
Measures	Units	SiG (60:10)	SiG (50:25)	SiG (35:45)	SiG (20:65)
Silicon-graphite electrode specifications					
Silicon content	%	60	50	35	20
Silicon loading	mg_{Si} cm^{-2}	0.64	0.47	0.46	0.43
FEC consumption per irr. capacity	$\mu mol\ mAh^{-1}{}_{irr}$	13.0	12.3	11.5	13.1
Lab-scale cell (85 $\mu L\ cm^{-2}$ electrolyte with 5 wt% FEC additive)					
Maximal irreversible capacity	$Ah_{irr}\ g^{-1}{}_{Si}$	5.8	8.3	9.1	8.4
Cycle lifetime acc. Figure 8a	#	>120	>120	>120	>120
Commercial-scale cell (5 $\mu L\ cm^{-2}$ electrolyte with 20 wt% FEC additive)					
Maximal irreversible capacity	$Ah_{irr}\ g^{-1}{}_{Si}$	1.4	1.9	2.2	2.0
Cycle lifetime acc. Figure 8a	#	20	25	30	25

capacities of 1.8–2.3 mAh cm^{-2}. By use of an FEC-containing electrolyte and capacitively oversized $LiFePO_4$ cathodes, we could clearly distinguish two degradation phenomena, which we described as silicon particle degradation and electrode degradation. While the former is mainly determined by the intrinsic properties of the silicon active material, such as particle size and morphology, as well as the amount of charge that is exchanged by the silicon particles, the electrode degradation mechanism depends not only on the silicon material but also on the electrode composition, i.e., the silicon/graphite ratio. Increasing the silicon content results in an increase of the number of interparticle contacts, e.g., silicon-silicon, which leads to a higher contact resistance. During discharge, i.e., in delithiated silicon electrodes, this phenomenon is even more pronounced because of a reduced contact pressure at these interfaces.

Based on our results from ^{19}F-NMR analysis we could demonstrate that the consumption of FEC after 120 cycles is independent of the graphite/silicon ratio and only depends on the total accumulated exchanged charge (i.e., sum of charge and discharge) experienced by the silicon. Based on this, we could show that: (i) the irreversible capacity loss correlates linearly with the decomposition of FEC on silicon, and can thus be used to estimate the extent of FEC consumption from the cycling data; (ii) the estimated volume of the FEC decomposition products increases with the silicon content and for all investigated SiG compositions largely exceeds the pore volume of the pristine electrodes, explaining the commonly observed swelling of silicon electrodes upon cycling; and (iii) the comparatively low molar quantity of FEC in commercial electrolytes is the most critical factor in determining the cycle life of silicon-based electrodes.

Acknowledgments

The German Federal Ministry for Economic Affairs and Energy is acknowledged for funding (Project “LiMo”, funding number 03ET6045D). Wacker Chemie AG is kindly acknowledged for providing the silicon nanoparticles. Susanne Cornfine and JEOL (Germany) GmbH are kindly acknowledged for supporting the SEM measurements. The authors also kindly thank Yelena Gorlin, Manu Patel, Qi He, and Anne Berger (all TUM) for fruitful discussions.

References

1. D. Andre, S.-J. Kim, P. Lamp, S. F. Lux, F. Maglia, O. Paschos, and B. Stiaszny, *J. Mater. Chem. A*, **3**(13), 6709 (2015).
2. O. Gröger, H. A. Gasteiger, and J.-P. Suchsland, *J. Electrochem. Soc.*, **162**(14), A2605 (2015).
3. V. L. Chevrier, L. Liu, D. B. Le, J. Lund, B. Molla, K. Reimer, L. J. Krause, L. D. Jensen, E. Figgemeier, and K. W. Eberman, *J. Electrochem. Soc.*, **161**(5), 783 (2014).
4. D. Ma, Z. Cao, and A. Hu, *Nano-Micro Lett*, **6**(4), 347 (2014).
5. M. N. Obrovac, L. Christensen, D. B. Le, and J. R. Dahn, *J. Electrochem. Soc.*, **154**(9), A849 (2007).
6. D. S. M. Iaboni and M. N. Obrovac, *J. Electrochem. Soc.*, **163**(2), 255 (2016).
7. M. N. Obrovac and V. L. Chevrier, *Chem. Rev.*, **114**, 11444 (2014).
8. R. Petibon, V. Chevrier, C. P. Aiken, D. S. Hall, S. Hyatt, R. Shunmugasundaram, and J. R. Dahn, *J. Electrochem. Soc.*, **163**(7), 1146 (2016).
9. J. O. Besenhard, J. Yang, and M. Winter, *J. Power Sources*, **68**, 87 (1997).
10. M. T. McDowell, S. W. Lee, J. T. Harris, B. A. Korgel, C. Wang, W. D. Nix, and Y. Cui, *Nano Lett*, **13**(2), 758 (2013).
11. R. Jung, M. Metzger, D. Haering, S. Solchenbach, C. Marino, N. Tsiouvaras, C. Stinner, and H. A. Gasteiger, *J. Electrochem. Soc.*, **163**(8), A1705 (2016).
12. V. Baranchugov, E. Markevich, E. Pollak, G. Salitra, and D. Aurbach, *Electrochem. commun.*, **9**(4), 796 (2007).
13. E. Markevich, K. Fridman, R. Sharabi, R. Elazari, G. Salitra, H. E. Gottlieb, G. Gershinsky, A. Garsuch, G. Semrau, M. A. Schmidt, and D. Aurbach, *J. Electrochem. Soc.*, **160**(10), A1824 (2013).
14. E. Markevich, G. Salitra, and D. Aurbach, *J. Electrochem. Soc.*, **163**(10), 2407 (2016).
15. Z. Du, R. A. Dunlap, and M. N. Obrovac, *J. Electrochem. Soc.*, **161**(10), 1698 (2014).
16. M. D. Fleischauer, M. N. Obrovac, J. D. Mcgraw, R. A. Dunlap, J. M. Topple, and J. R. Dahn, *J. Electrochem. Soc.*, **153**(3), 484 (2006).
17. B. Fuchsbichler, C. Stangl, H. Kren, F. Uhlig, and S. Koller, *J. Power Sources*, **196**(5), 2889 (2011).
18. C.-H. Yim, F. M. Courtel, and Y. Abu-Lebdeh, *J. Mater. Chem. A*, **1**(5), 8234 (2013).
19. T. Yim, S. J. Choi, J.-H. Park, W. Cho, Y. N. Jo, T.-H. Kim, and Y.-J. Kim, *Phys. Chem. Chem. Phys.*, **17**(4), 2388 (2014).
20. M. Ko, S. Chae, and J. Cho, *ChemElectroChem*, **2**(11), 1645 (2015).
21. F. Luo, B. Liu, J. Zheng, G. Chu, K. Zhong, H. Li, X. Huang, and L. Chen, *J. Electrochem. Soc.*, **162**(14), A2509 (2015).
22. M. T. McDowell, S. W. Lee, W. D. Nix, and Y. Cui, 4966 (2013).
23. N. Dupré, P. Moreau, E. De Vito, L. Quazuguel, M. Boniface, A. Bordes, C. Rudisch, P. Bayle-Guillemaud, and D. Guyomard, *Chem. Mater.*, **28**(8), 2557 (2016).
24. N. Delpuech, N. Dupre, P. Moreau, J. S. Bridel, J. Gaubicher, B. Lestriez, and D. Guyomard, *ChemSusChem*, **9**(8), 841 (2016).
25. M. Klett, J. A. Gilbert, S. E. Trask, B. J. Polzin, A. N. Jansen, D. W. Dees, and D. P. Abraham, *J. Electrochem. Soc.*, **163**(6), A875 (2016).
26. M. Klett, J. A. Gilbert, K. Z. Pupek, S. E. Trask, and D. P. Abraham, *J. Electrochem. Soc.*, **164**(1), 6095 (2017).
27. S. E. Trask, K. Z. Pupek, J. A. Gilbert, M. Klett, B. J. Polzin, A. N. Jansen, and D. P. Abraham, *J. Electrochem. Soc.*, **163**(3), A345 (2016).
28. C. Erk, T. Brezesinski, H. Sommer, R. Schneider, and J. Janek, *ACS Appl. Mater. Interfaces*, **5**(15), 7299 (2013).
29. J. H. Ryu, J. W. Kim, Y. Sung, and S. M. Oh, *Electrochem. Solid State Lett.*, **7**(10), 306 (2004).
30. T. Yoon, C. C. Nguyen, D. M. Seo, and B. L. Lucht, *J. Electrochem. Soc.*, **162**(12), A2325 (2015).
31. M. Wetjen, R. Jung, D. Pritzl, and H. A. Gasteiger, *ECS Meet*, **230** (2016), Abstr. #280.
32. E. Markevich, K. Fridman, R. Sharabi, R. Elazari, G. Salitra, H. E. Gottlieb, G. Gershinsky, A. Garsuch, G. Semrau, M. a Schmidt, and D. Aurbach, *J. Electrochem. Soc.*, **160**(10), A1824 (2013).
33. T. Marks, S. Trussler, A. J. Smith, D. Xiong, and J. R. Dahn, *J. Electrochem. Soc.*, **158**(1), A51 (2011).
34. A. V Plakhotnyk, L. Ernst, and R. Schmutzler, *J. Fluor. Chem.*, **126**(1), 27 (2005).
35. R. Petibon, V. L. Chevrier, C. P. Aiken, D. S. Hall, S. R. Hyatt, R. Shunmugasundaram, and J. R. Dahn, *J. Electrochem. Soc.*, **163**(7), A1146 (2016).
36. K. W. Schroder, H. Celio, L. J. Webb, and K. J. Stevenson, *J. Phys. Chem. C*, **116**, 19737 (2012).
37. T. Ohzuku, Y. Iwakoshi, and K. Sawai, *J. Electrochem. Soc.*, **140**(9), 2490 (1993).
38. T. Swamy and Y.-M. Chiang, *J. Electrochem. Soc.*, **162**(13), A7129 (2015).

39. C. Xu, F. Lindgren, B. Philippe, M. Gorgoi, F. Björefors, K. Edström, and T. Gustafsson, *Chem. Mater.*, **27**(7), 2591 (2015).
40. T. Jaumann, J. Balach, M. Klose, S. Oswald, U. Langklotz, A. Michaelis, J. Eckert, and L. Giebeler, *Phys. Chem. Chem. Phys.*, **17**(38), 24956 (2015).
41. D. Aurbach, *J. Power Sources*, **89**, 206 (2000).
42. T. Placke, S. Rothermel, O. Fromm, P. Meister, S. F. Lux, J. Huesker, H. Meyer, and M. Winter, *J. Electrochem. Soc.*, **160**, A1979 (2013).
43. M. N. Obrovac and L. Christensen, *Electrochem. Solid-State Lett.*, **7**(5), A93 (2004).
44. J. Li and J. R. Dahn, *J. Electrochem. Soc.*, **154**(3), A156 (2007).
45. D. Aurbach, E. Zinigrad, Y. Cohen, and H. Teller, *Solid State Ionics*, **148**, 405 (2002).
46. M. Gauthier, T. J. Carney, A. Grimaud, L. Giordano, N. Pour, H. Chang, D. P. Fenning, S. F. Lux, O. Paschos, C. Bauer, F. Maglia, S. Lupart, P. Lamp, and Y. Shao-horn, *J. Phys. Chem. Lett.*, **6**, 4653 (2015).
47. J. Erlebacher, M. J. Aziz, A. Karma, N. Dimitrov, and K. Sieradzki, *Nature*, **410**, 450 (2001).
48. M. Wetjen, S. Solchenbach, D. Pritzl, J. Hou, V. Tileli, and H. A. Gasteiger, Manuscript in preparation.
49. D. Pritzl, S. Solchenbach, M. Wetjen, and H. A. Gasteiger, *J. Electrochem. Soc.*, **164** (12), A2625 (2017).
50. X. Cheng, R. Zhang, C. Zhao, F. Wei, J. Zhang, and Q. Zhang, *Adv. Sci.*, **3**, 1 (2016).
51. E. Peled, D. Golodnitsky, and G. Ardel, *J. Electrochem. Soc.*, **144**(8), 208 (1997).
52. K. Schroder, J. Alvarado, T. A. Yersak, J. Li, N. Dudney, L. J. Webb, Y. S. Meng, and K. J. Stevenson, *Chem. Mater.*, **27**(16), 5531 (2015).
53. D. Mazouzi, N. Delpuech, Y. Oumellal, M. Gauthier, M. Cerbelaud, J. Gaubicher, N. Dupré, P. Moreau, D. Guyomard, L. Roué, and B. Lestriez, *J. Power Sources*, **220**, 180 (2012).
54. M. Wetjen, G. Hong, S. Solchenbach, D. Pritzl, and H. A. Gasteiger, Manuscript in preparation.